High-resolution contrast-enhanced microCT reveals the true three-dimensional morphology of the murine placenta

Katrien De Clercq[a,b,c], Eleonora Persoons[a,b,c], Tina Napso[d], Catherine Luyten[a], Tatjana N. Parac-Vogt[e], Amanda N. Sferruzzi-Perri[d], Greet Kerckhofs[f,g,h,1], and Joris Vriens[a,1,2]

[a]Laboratory of Endometrium, Endometriosis & Reproductive Medicine, Department of Development and Regeneration, Gynecology-Pediatrics and Urology Research Group (G-PURE), Katholieke Universiteit (KU) Leuven, 3000 Leuven, Belgium; [b]Laboratory of Ion Channel Research, Department of Cellular and Molecular Medicine, KU Leuven, 3000 Leuven, Belgium; [c]Vlaams Instituut voor Biotechnologie (VIB) Centre for Brain & Disease Research, 3000 Leuven, Belgium; [d]Centre for Trophoblast Research, Department of Physiology, Development and Neuroscience, University of Cambridge, Cambridge CB2 3EG, United Kingdom; [e]Molecular Design and Synthesis, Department of Chemistry, KU Leuven, 3000 Leuven, Belgium; [f]Biomechanics Laboratory, Institute of Mechanics, Materials, and Civil Engineering, Université Catholique de Louvain, 1348 Louvain-la-Neuve, Belgium; [g]Department of Materials Science and Engineering, KU Leuven, 3000 Leuven, Belgium; and [h]Prometheus, Division of Skeletal Tissue Engineering, KU Leuven, 3000 Leuven, Belgium

Genetic engineering of the mouse genome identified many genes that are essential for embryogenesis. Remarkably, the prevalence of concomitant placental defects in embryonic lethal mutants is highly underestimated and indicates the importance of detailed placental analysis when phenotyping new individual gene knockouts. Here we introduce high-resolution contrast-enhanced microfocus computed tomography (CE-CT) as a nondestructive, high-throughput technique to evaluate the 3D placental morphology. Using a contrast agent, zirconium-substituted Keggin polyoxometalate (Zr-POM), the soft tissue of the placenta (i.e., different layers and cell types and its vasculature) was imaged with a resolution of 3.5 μm voxel size. This approach allowed us to visualize and study early and late stages of placental development. Moreover, CE-CT provides a method to precisely quantify placental parameters (i.e., volumes, volume fraction, ratio of different placental layers, and volumes of specific cell populations) that are crucial for statistical comparison studies. The CE-CT assessment of the 3D morphology of the placentas was validated (i) by comparison with standard histological studies; (ii) by evaluating placentas from 2 different mouse strains, 129S6 and C57BL/6J mice; and (iii) by confirming the placental phenotype of mice lacking phosphoinositol 3-kinase (PI3K)-p110α. Finally, the Zr-POM–based CE-CT allowed for inspection of the vasculature structure in the entire placenta, as well as detecting placental defects in pathologies characterized by embryonic resorption and placental fusion. Taken together, Zr-POM–based CE-CT offers a quantitative 3D methodology to investigate placental development or pathologies.

murine placental development | poly-oxometalate–based contrast-enhanced microCT | 3D morphological assessment | placental defects

The laboratory mouse remains the superior model to assess gene function in embryogenesis. Up to one-third of individual gene knockouts result in fetal demise and thus nonviable offspring (1, 2). Unfortunately, the contribution of placental defects in lethal strains is often disregarded, resulting in the misinterpretation of gene function in the developing embryo. Recently, a systematic phenotyping effort of extraembryonic tissues revealed that placental abnormalities are highly prevalent in lethal or subviable mouse mutants and implies that defects in placentation have been highly underestimated (3, 4). In addition, increasing evidence suggests that improper placental functioning and subsequent intrauterine growth restriction can increase the susceptibility for metabolic diseases such as type 2 diabetes and hypertension (5, 6). Moreover, placental phenotypes are often concomitant with defects within the embryo, including neuronal and vascular development, emphasizing the importance of including the analysis of the placenta when embryonic or perinatal lethality is observed.

The placenta is an extraordinary, albeit transient organ that functions as surrogate fetal lungs, kidneys, and gut. Hence, defects in the proper formation of this extraembryonic tissue can result in early embryonic lethality. Moreover, the placenta produces and secretes a variety of hormones to adapt the maternal metabolism to comply with the needs of the growing conceptus (7). Murine placentation commences during implantation, around embryonic day 4 (E4), with the formation of the extraembryonic lineages and inverted yolk sac. The vitelline circulation of the yolk sac is paramount in the provision of nutrients to the growing conceptus. During the second half of gestation, fetal growth mainly depends on the chorioallantoic placenta, although the yolk sac continuous to function until term (8). After chorioallantoic fusion at E8.5, branching morphogenesis is initiated, and by E12.5, fetomaternal exchange is established as evidenced by the presence of maternal blood in the placental labyrinth at this stage. The mature murine placenta consists of 3 clearly distinguishable layers, i.e., the labyrinth, the junctional zone, and the maternal decidua (9). The labyrinth is the innermost and largest layer in which the juxtaposition of the maternal and fetal

Significance

During pregnancy, the placenta functions as surrogate fetal lungs, kidneys, and gut. Proper placental functioning is therefore paramount during embryonic development. Indeed, placental defects are highly prevalent in mouse mutants showing embryonic death. Here we validate a contrast agent that allows development of the intact placenta to be visualized using microfocus computed topography. This technique enables an initial 3D inspection of the overall placental structure and provides the possibility to quantify different compartments in the placenta. Moreover, the nondestructive nature of this contrast agent permits further histological processing of the same sample when defects are observed.

circulation allows an optimal exchange of nutrients and gas over the interhaemal membrane. The junctional zone comprises spongiotrophoblast and glycogen cells and fulfils important metabolic and endocrine functions. This layer is separated from the maternal decidua by a layer of secondary trophoblast giant cells. The maternal decidua is the sole layer that is derived from maternal tissues and is important for providing nutrition during early developmental stages. Interestingly, the relative size and appearance of these layers changes throughout gestation to support fetal needs. As such, the relative size of the labyrinth increases, and its structure becomes more complex to allow the exponential growth of the fetus toward term. In contrast, the size of the junctional zone obtains its maximum at the beginning of the third semester and gradually decreases thereafter (10, 11).

Defects in the formation of either of the placental layers can result in placental insufficiency and thus adversely affect fetal development. Determining the size of the different layers during placentation is therefore considered as a first important step when phenotyping new mutant models. Conventionally, these measurements are assessed by standard histological protocols (12), complemented with additional histologic stains to classify cellular tissue composition. Although this technique has proven to be a valuable tool owing to its high discriminative power and accuracy at cellular level, it is subjected to sampling bias. Due to the complex architecture of the placenta, histological examinations also require a multitude of sections to be analyzed before results can be conclusive. Moreover, tissue shrinkage is inherent to embedding procedures and limits the assessment of the correct volume measures. Random sampling and statistical algorithms used in stereology offer an elegant solution to generate 3D quantities from 2D histological sections (13, 14) and have been successfully used in the field of human and murine placentology (10, 15). To date, the process of exhausting sectioning remains the basis for exploring embryonic and placental development and allows for detailed investigations when combined with protein or RNA expression studies. However, it is labor-intensive and time-consuming when morphological information about gross placental morphology is required. Therefore, the field of placental phenotyping would benefit from novel techniques that allow a fast and accurate inspection of the overall placental structure.

Microfocus computed X-ray tomography (microCT) is a recent technique that allows 3D quantification of mineralized samples with high contrast and high resolution, although without sample destruction (16, 17). Moreover, it is an established method for vasculature analysis and blood flow modeling by the perfusion of intravascular contrast agents (18). As such, previous studies have used this technique to identify the fetoplacental vasculature of rodents and humans by injecting the contrast agent into the vessels of the umbilical cord (19–24). Additionally, the human fetoplacental vasculature was imaged by 3D microCT by exploiting vascular casting techniques (25). Recently, the interest in contrast-enhanced microCT (CE-CT) has increased as it can also be used to visualize soft tissues, such as muscles and adipocytes, by incubating whole tissue samples in contrast agents (26). This approach was successfully used to visualize the developing embryo using an iodine-based contrast agent (27). However, the morphology of extraembryonic tissues has so far not been assessed. Therefore, we aimed to determine whether CE-CT could be extended for the 3D morphological assessment of developing placentas. Polyoxometalate (POM)-based contrast agents have previously been used to visualize the soft tissues surrounding bone, such as adipose tissue and blood vessels, without tissue destruction (28). Here we used zirconium-substituted Keggin polyoxometalate (Zr-POM), which has a similar binding efficiency to collagen type I, type II, fibrin, and rat tendon as the previously reported Hf-POM (28). These findings indicate that Zr-POM does not alter the chemical structure of these proteins, which is an important advantage compared with the conventional contrast agents, e.g., phosphotungstic acid (PTA) or iodine-based contrast agents such as Lugol (29).

Using Zr-POM with CE-CT, we evaluated whether we could (*i*) visualize the early stages of embryonic and placental development; (*ii*) image the morphological structure of the definitive murine placenta, including its 3 layers, using standard histological staining techniques as a reference; (*iii*) precisely quantify the volumes of placental layers; (*iv*) confirm earlier reported placental morphologies of 2 mouse strains (129S and C57BL/6J) (30) and of phosphoinositol 3-kinase (PI3K) mutants (31); (*v*) investigate the vasculature in the intact placenta; and (*vi*) study placental pathologies like embryo resorption and placental fusion.

Results

Visualization of Early Placental Development. To visualize the early stages of embryonic and placental development, the entire uterine horn was isolated at different time points during early gestation and incubated in Zr-POM. At E7.5, the typical features of the late primitive streak embryo were distinguishable (Fig. 1). The amniotic cavity was subdivided into 3 cavities, i.e., the ectoplacental, exocoelomic, and amniotic cavity. Moreover, elongation of the allantoic bud, starting at the amnion toward the chorion was observed. These hallmarks were suggestive for Theiler stage 11 of the mouse development (32). Interestingly, the use of Zr-POM–based CE-CT allowed us to distinguish the mesometrium, myometrium, the decidua, and the uterine lumen surrounded by a single layer of epithelial cells and vascular sinuses in the uterine horn.
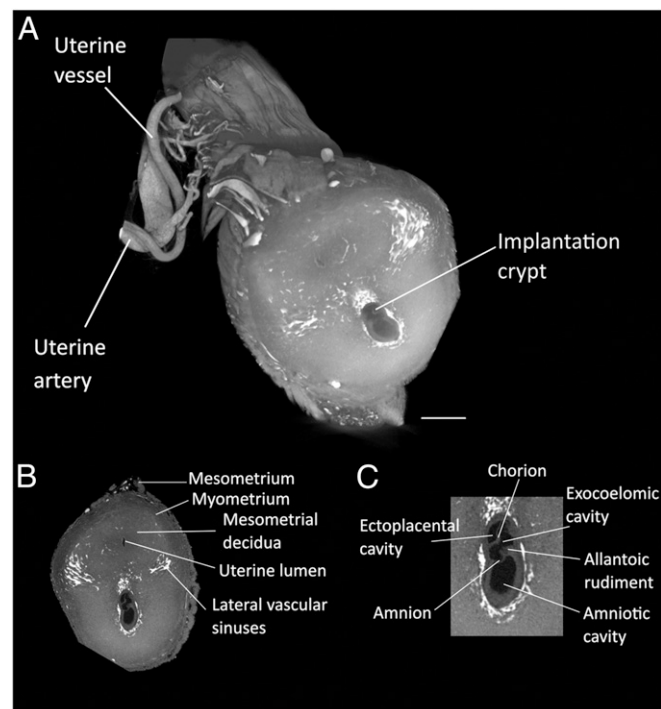

Fig. 1. Visualization of early implantation site (E7.5). (*A*) Zr-POM-based CE-CT 3D rendering on an early implantation site at E7.5. The uterine vasculature can be recognized including the uterine artery, accompanied by the uterine vein that splits into the arcuate artery and then ramifies into the radial arteries and subsequently the spiral arteries. (*B*) CE-CT image of a cross section of the uterine wall allows the visualization of the typical features of a primitive streak embryo (Theiler stage 11) including the mesometrium, myometrium, endometrium, uterine lumen, and vascular sinuses. (*C*) Magnification of the implanting embryo with the ectoplacental, exocoelomic and amniotic cavity, the chorion, the amnion, and the allantois. Samples obtained from 129S6 mice. (Scale bar, 500 μm.)

De Clercq et al.

At E8.5, an unturned embryo was observed in which neural folding did not initiate yet (*SI Appendix*, Fig. S1 and Movie S1). Moreover, primary trophoblast giant cells surrounding the embryo could be visualized. In this sample, at least 4 somites were detected, and the allantois contacted the chorion, suggesting that the embryo is at the end of Theiler stage 12.

At E9.5, embryo turning and chorioallantoic attachment could be investigated (Fig. 2 and Movie S2). In Fig. 2*A* (2D view) and Fig. 2*B* (3D histology), a certain degree of closure of the neural fold was detected to form the posterior and anterior neuropore. Moreover, the forelimb bud and the second branchial arch were visible. Furthermore, the first steps in heart development could be distinguished by the detection of primitive blood vessels. As such, we observed an almost completed turned embryo with 15 somite pairs, indicating that embryo development was at Theiler stage 14. In contrast, embryonic development from a littermate was seemingly arrested at the end of Theiler stage 12 (Fig. 2*C*). Although chorioallantoic attachment occurred, embryo turning did not ensue since the neural fold was still facing the center of the implantation crypt, the yolk sac did not occupy the complete amniotic cavity, the second branchial arch was absent, and somites were not readily detectable. Altogether, these analyses showed the potency of the Zr-POM–based CE-CT to visualize the hallmarks of early embryonic and placental development.

Visualization of the Mature Placenta and Validation by Histology. In the placenta at E10.5–E11.5, the structures of the definitive chorioallantoic placenta started to become evident. However,
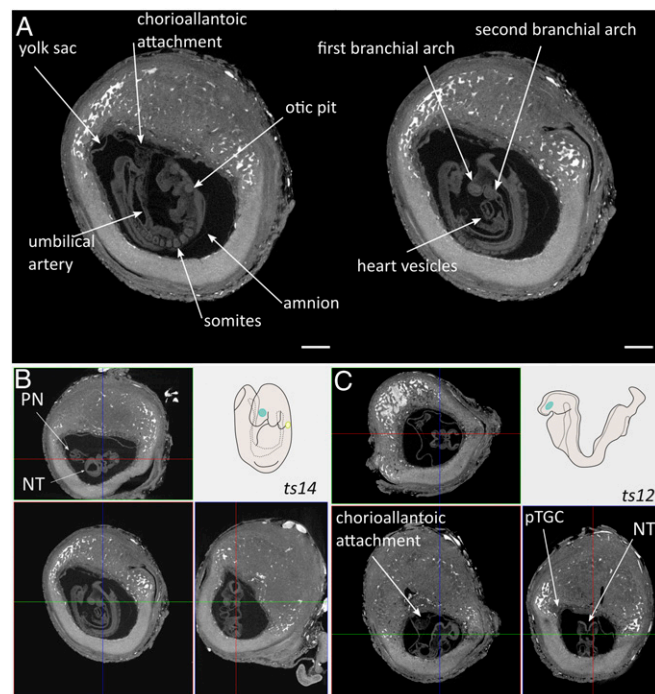

Fig. 2. Imagining and staging of E9.5 embryo. (*A*) CE-CT cross sections showing typical features of E9.5 including chorioallantoic attachment and the presence of the umbilical artery, 12–15 somites, formation of the otic pit, the presence of the first and the second branchial arch, and the initiation of heart formation. (Scale bar, 500 μm.) (*B* and *C*) Staging E9.5 embryos by 3D histology of CE-CT dataset giving coronal (*Upper*), trans axial (*Lower Left*) and sagittal (*Lower Right*) sections of the process of embryonic turning in uncompromised (*B*) and compromised (*C*) embryonic development, compared with schematic representation of Theiler stage 14 (*B*, *Upper Right*) and Theiler stage 12 (*C*, *Upper Right*). Samples obtained from 129S6 mice. pTGC, primary trophoblast giant cell; PN, posterior neuropore; NT, neural tube.

the labyrinth could not be distinguished from the junctional zone at these gestational ages using Zr-POM–based CE-CT (Fig. 3). Nevertheless, a clear demarcation between the fetal placenta and the maternal decidua with the mesometrial lymphoid aggregate of pregnancy (MLAp) was apparent.

From E12.5 onward, the specific morphological features of the placenta became more obvious, allowing the discrimination of different placental layers, of which the appearance and size drastically changed over time (Fig. 3 and Movie S3). To confirm the identity of morphological structures observed in CE-CT images, samples from E14.5 and E18.5 that were formerly incubated with Zr-POM were further processed for immune histology. In line with previous findings (28), Zr-POM did not interfere with subsequent stains, nor did it affect the specificity (*SI Appendix*, Figs. S2 and S3*A*), providing the possibility of a one-on-one comparison. Notably, the difference in cellular composition between the placental layers was sufficient to readily distinguish the gross placental morphology on CE-CT images. At E14.5, the maternal decidua consists of decidualized stromal cells and uterine NK cells, which are glycogen positive but negative for cytokeratin. The junctional zone mainly comprises spongiotrophoblast and glycogen trophoblast cells. The former are densely packed cells, while the latter are highly vacuolated cells with few organelles that grow in rounded islets (33). Interestingly, this substantial difference in cellular composition made it possible to discriminate these cell populations in CE-CT images, which was confirmed on the corresponding PAS stained section (*SI Appendix*, Fig. S3*B*). Interestingly, isolated inclusions of the junctional zone into the labyrinth, containing both glycogen and spongiotrophoblast cells, could be observed with Zr-POM–based CE-CT (*SI Appendix*, Fig. S3*A*, yellow arrow) (34). Markedly, comparing CE-CT images with histology revealed a high affinity of Zr-POM for blood. This advantage enabled the tracking of spiral arteries that diverge into maternal canals, which branch near the chorionic plate (Fig. 3, yellow arrows, and Movie S3). In addition, maternal veins that transverse the junctional zone to drain the maternal blood into venous sinuses (*SI Appendix*, Fig. S3*B*, arrowheads) provided a helpful landmark to delineate the boundaries between the junctional zone and the decidua.

A strong correlation between the 2D labyrinth area quantified on histological sections and the area quantified on the corresponding CE-CT images proved that specific regions can be easily distinguished on CE-CT images (Spearman correlation coefficient 0.83, $R^2 = 0.67$, $P < 0.01$; *SI Appendix*, Fig. S4). The ratio of the labyrinth area to junctional zone area (Lb:Jz ratio) is a measure that is used to indicate the composition of the placenta. However, 360° sectioning around the midline using CE-CT–based 3D histology revealed substantial differences in placental structures in different sections. To exemplify, the Lb:Jz ratio was determined in E16.5 placentas of littermates on sections containing a maternal canal, an indication of a midline sections (35, 36). Notably, the 2D Lb:Jz ratio of perpendicular sections (sagittal and transaxial) with the same maternal canal present were markedly different (4.3 vs. 2.4 at location 1 and 3.2 vs. 2.3 at location 2) (*SI Appendix*, Fig. S3*C*). In contrast, differences between sagittal and transaxial sections were less variable in a littermate, even though these sections were farther away from the middle of the placenta and from each other (3.1 vs. 3.0 in location 1 and 4.3 vs. 3.3 in location 2) (*SI Appendix*, Fig. S3*D*). Given the substantial variation in placental structure between sections (Movie S3), quantification of placental regions would benefit from whole-organ 3D measurements and encouraged us to quantify the volumes of the different placental layers.

Quantification of the Mature Placenta by Zr-POM–Based CE-CT. The placental 3D volume was precisely quantified using Zr-POM–based CE-CT without the need for extensive sectioning. Fluctuations in 3D placental volumes during gestation were similar to placental weights recorded immediately following dissection
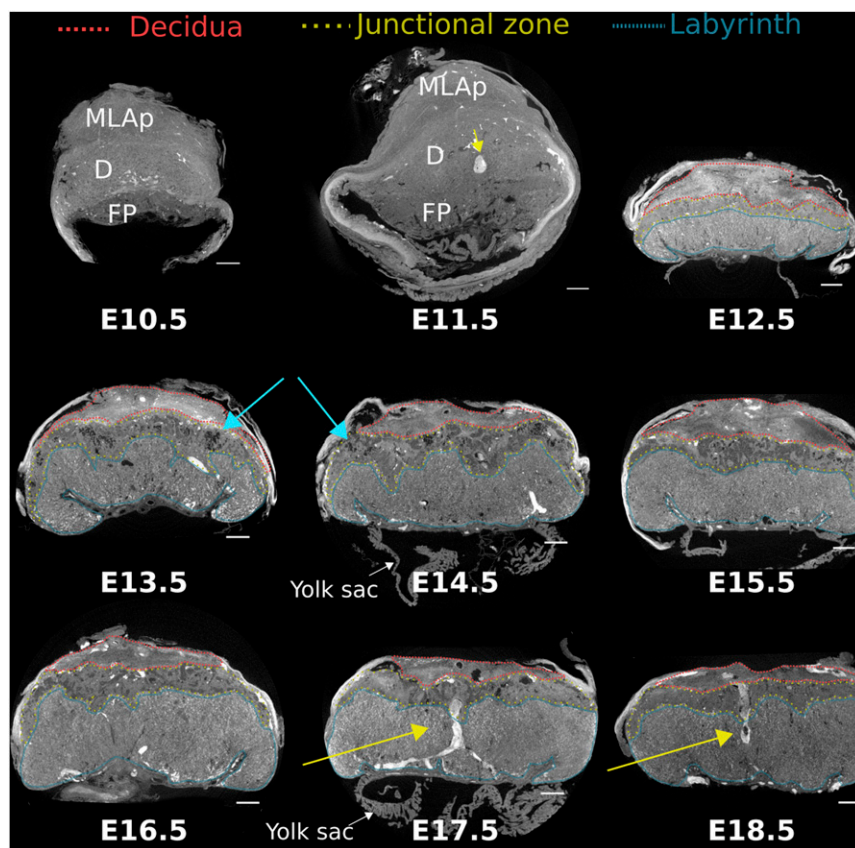
Fig. 3. Cross-sectional CE-CT images from E10.5–E18.5 placentas, with the different layers indicated. MLAp, mesometrial lymphoid aggregate of pregnancy; D, decidua (red); FP, fetal placenta; junctional zone (yellow); labyrinth (blue); blue arrow, lacunae in junctional zone; yellow arrow, maternal canal. Samples obtained from 129S6 mice. (Scale bar, 500 μm.)

(Fig. 4 *A* and *B* and *SI Appendix,* Table S1). This resulted in a strong correlation between placental weight and 3D volume (Pearson correlation coefficient 0.77, $R^2 = 0.6$, $P < 0.001$; Fig. 4*C*). The volumetric mass density of the placentas was calculated as weight per volume but did not show significant alterations over time. Nevertheless, a subtle difference at E14.5 was observed as placental weight increased by 32%, whereas placental volume increased by 17% between E13.5 and E14.5 (Fig. 4*D*). Altogether, Zr-POM–based CE-CT allowed for a fast and reliable quantification of placental volume and density.

Given the accuracy of Zr-POM–based CE-CT to discriminate the different placental layers, the volume and volume fractions of the different layers were determined throughout gestation (Fig. 4 *E* and *F* and *SI Appendix,* Table S2). In line with literature (10), the volume and volume fraction of the maternal decidua drastically decreased toward term, from 7.1 ± 0.3 mm^3 to 3.5 ± 0.4 mm^3, relating to $14.4 \pm 4.8\%$ and $5.9 \pm 0.8\%$, respectively. In contrast, the volume and volume fraction of the labyrinth significantly increased daily, indicating its continuous growth and development. As such, the absolute labyrinth volume almost doubled (19.7 ± 3.1 mm^3 at E13.5 to 37.2 ± 4.7 mm^3 at E18.5) and was reflected in a significant increase in volume fraction from $40.1 \pm 2.2\%$ to $61.8 \pm 5.1\%$ of the placenta, respectively. Instead, the volume of the junctional zone reached its maximum at E15.5 (11.3 ± 1.8 mm^3 at E13.5 until 14.7 ± 3.2 mm^3 at E15.5), whereas the volume fraction of the junctional zone peaked at E14.5 ($22.8 \pm 3.5\%$ to $24.7 \pm 1.7\%$). Thereafter, volume fraction significantly decreased toward term, probably because of the massive migration of glycogen cells into the decidua before term (8.3 ± 1.4 mm^3 relating to $13.8 \pm 1.5\%$ at E18.5). As shown previously (*SI Appendix,* Fig. S3 *C* and *D*), the 2D Lb:Jz ratios showed intersample and intrasample variations and would benefit from 3D volumetric ratios. The 3D Lb:Jz ratios significantly increased over time due to the expansion of the labyrinth volume, from 1.76 ± 0.08 at E13.5 to 4.59 ± 0.45 at E18.5

(Fig. 4*G*). Hence, Zr-POM–based CE-CT permitted an initial analysis of placental structures, which requires less time compared with standard histology (*SI Appendix,* Table S3).

Comparison of the CE-CT image with the corresponding histological sections revealed that different cell types of the junctional zone could be distinguished (*SI Appendix,* Fig. S3*B*). Therefore, 3D image analysis was performed on the junctional zone to quantify the relative proportion of glycogen cells and spongiotrophoblast cells. The volume fraction of glycogen trophoblast cells was at its maximum between E13.5 and E15.5, occupying $48.5 \pm 1.8\%$ of the junctional zone (Fig. 4*H*), where after it significantly reduced to $12.7 \pm 3.4\%$ of the junctional zone near term. In contrast, the volume fraction of the spongiotrophoblast drastically increased from $38.9 \pm 3.3\%$ to $87.4 \pm 3.4\%$. Notably, lacuna, which were evident at earlier stages studied, disappeared from the junctional zone at E15.5 (Fig. 3, blue arrows, and Fig. 4*H*). These findings indicated that Zr-POM–based CE-CT offers the unique potential to quantify the structure and composition of the junctional zone in 3D, resulting in a more rapid estimation of the junctional zone composition.

Zr-POM–Based CE-CT to Study Placental Phenotypes and Pathologies.

Within-species differences in placental development. In biological studies, the C57BL/6J and 129S6 inbred strains are considered the standard laboratory mouse models to study the effect of single gene mutation. However, placental phenotypes and thus embryonic lethality are often strain dependent, which might prompt backcrossing to the other strain. Remarkably, striking differences exist in the placental morphology between both mouse strains, including the relative distribution of the placental layers (30). To illustrate the validity of Zr-POM–based CE-CT, placentas derived from 2 different mice strains were compared at different time points of gestation (E14.5 and E18.5) (Fig. 5*A*). Although fetal weight was similar (Fig. 5*B*), placental weights
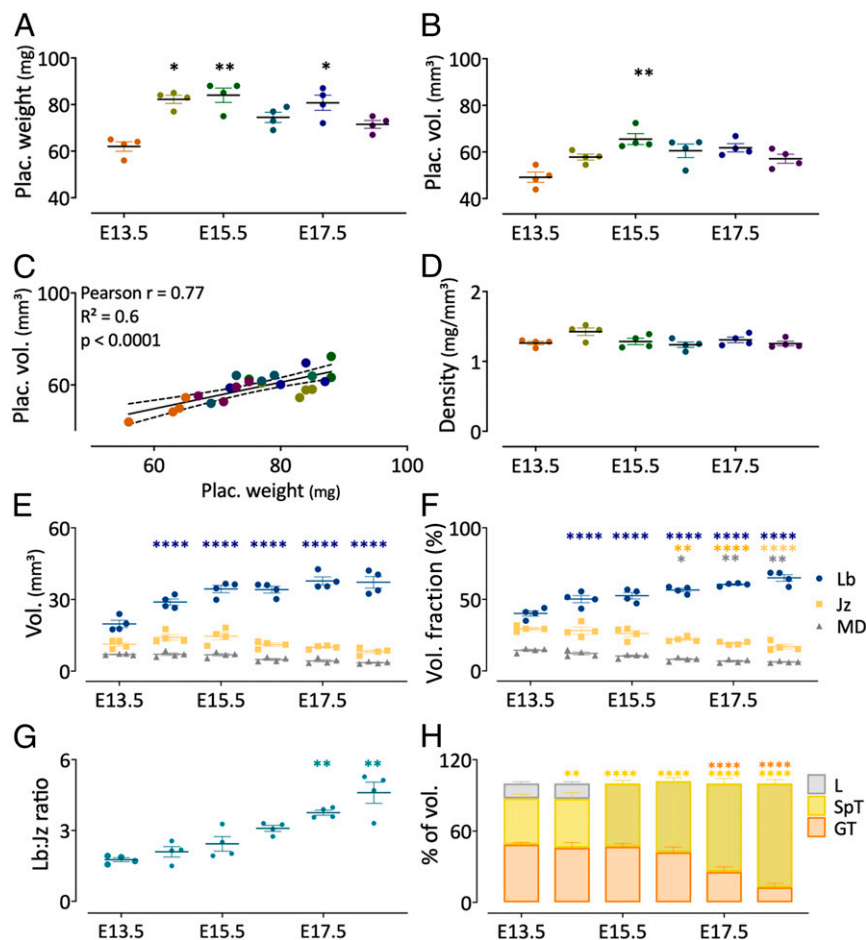
Fig. 4. Quantification of placental parameters of 129S6 mice through gestation. (*A*) Placental weight throughout pregnancy. (*B*) Placental volume assessed with Zr-POM–based CE-CT. (*C*) Correlation between weight and volume, Pearson correlation test. (*D*) Placental density, calculated as placental weight per placental volume, throughout gestation. (*E*) Volume and (*F*) volume fraction of the placental layers on different days of gestation. (*G*) Labyrinth:junctional zone (Lb:Jz) ratio through gestation (arbitrary units) (*H*) CE-CT–based 3D analysis of the proportion of lacunae (L), glycogen cells (GT), and spongiotrophoblasts (SpT) in the junctional zone throughout gestation. Data are shown as mean ± SEM. *$P < 0.05$, **$P < 0.01$, ***$P < 0.001$. Kruskal–Wallis with Dunn's multiple testing correction compared with E13.5 for *A*–*G*, two-way ANOVA adjusted with Dunnet's multiple testing correction compared with E13.5 for *H*. N = 4 samples from 3 to 4 litters per gestational day.

were significantly higher by ~25% at E14.5 and/or E18.5 in C57BL/6J mice compared with 129S6 mice (Fig. 5*C*). As such, placental efficiency, defined as fetal:placental weight ratios, was ~10% higher at E14.5 and significantly higher by ~20% at E18.5 (Fig. 5*D*). The difference in placental size imposed a different CE-CT scanning resolution of 3.5 μm for 129S6 compared with 4.5 μm for C57BL/6J mice. In line with placental weight, the volume of the C57BL/6J placenta was ~30% larger at E14.5 and ~20% at E18.5 (Fig. 5*E*). While labyrinth volume at E14.5 and E18.5 was similar for 129S6 and C57BL/6J, the volume of the junctional zone was significantly larger in C57BL/6J placentas (Fig. 5 *F* and *G*). Given the overall smaller placental volume of 129S6 placenta, this difference resulted in an overall altered placental structure regarding volume densities. As such, the volume fraction of the junctional zone at E14.5 and E18.5 of C57BL/6J mice was significantly larger compared with 129S6 mice, whereas the volume fraction of the labyrinth was significantly smaller (Fig. 5*G*). Consistent with this, visual inspection of the placentas from both strains revealed that the junctional zone of C57BL/6J placentas covered the whole labyrinth until the chorionic plate, whereas the junctional zone was limited to the upper part of the 129S6 placentas (Fig. 5*A*). Thus, the difference in placental efficiency near term might be attributed to greater proportions of the labyrinth in 129S6 placentas compared with C57BL/6J placentas

(61.2 ± 5.1% vs. 45.1 ± 3.5%, respectively). Nevertheless, at E18.5, placental volumes of male and female C57BL6/J fetuses were not significantly different (Fig. 5*H*). Moreover, volume fractions of the labyrinth and the junctional zone were similar in placentas from male and female fetuses (Fig. 5*I*).

Placental phenotype of PI3K mutant mice. To assess whether CE-CT could be used to identify placental defects, the phenotype of the placenta heterozygous deficient in PI3K p110α was inspected. PI3K p110α plays a major role in mediating the growth and metabolic effects of the fetoplacental growth factors, insulin and insulin-like growth factors. Homozygous disruption of the p110α gene results in embryonic lethality, whereas heterozygous disruption (α/+) leads to viable pups that are growth restricted near term (31). Recently, the placental phenotypes of α/+ fetuses born from crosses of α/+ males and wild-type dams was established using histology and stereology (31). Here we used CE-CT to validate differences in gross placental morphology observed between α/+ fetuses and wild-type littermates at E16 (Fig. 6*A*). In line with the significant reduction in placental weight described previously (31), the 3D volume of α/+ mutant placentas was significantly less by 15%, compared with wild-type littermates (74.8 ± 6.7 mm³ vs. 87.6 ± 6.5 mm³, $P = 0.0006$; Fig. 6 *B* and *C*). Also consistent with previous findings (31), α/+ mutant compared with wild-type placentas showed a 20% reduction in the absolute volume of the

labyrinth zone (27.5 ± 2.1 mm^3 vs. 34.6 ± 1.3 mm^3, $P = 0.0004$) and no difference in the absolute volume of the junctional zone (25.6 ± 4.3 mm^3 vs. 25.4 ± 5.3 mm^3; Fig. 6D). Consequently, the Lb:Jz ratio was significantly altered in α/+ mutant versus wild-type placentas (Fig. 6E). Of note, the volume of the labyrinth zone was $41.3 \pm 2.9\%$ larger than the junctional zone in wild-type littermates but only $9.7 \pm 1.8\%$ larger in α/+ placentas. As such, wild-type placentas consisted of $39.7 \pm 3.2\%$ labyrinth and $28.9 \pm 5.2\%$ junctional zone, whereas α/+ placentas consisted of $37.2 \pm 2.3\%$ labyrinth and $34.4 \pm 3.9\%$ junctional zone. Hence, α/+ placentas consist of a significantly larger junctional zone volume fraction. Taken together, our findings validate the use of CE-CT in identifying defects in placental volumes and structure.

Additional Prospects of Zr-POM–Based CE-CT Phenotyping of Placentas.
Placental vasculature. Interestingly, a very strong contrast was observed for blood inside the fetal and maternal vessels, suggesting that Zr-POM has a high affinity for certain components inside blood. This feature offered the possibility to visualize and analyze properties of blood-filled vessels in intact tissues. Indeed, the 3D images can be rotated and sectioned in such a way that the diameter of the maternal canals at the junctional–labyrinth border can be measured. Additionally, a thickness distribution of the uteroplacental vessels can be assessed, giving an indication of the diameter through the length of the vessel (*SI Appendix*, Fig. S5A). Using this approach, focal hemorrhage spots or ruptures of the vasculature were easily identified (*SI Appendix*, Fig. S5B). Moreover, we found that the diameter of the maternal canal increased by 70% from E13.5 to E17.5 (*SI Appendix*, Fig. S5 C and D), which confirmed earlier observations (37). However, the vessels lacking
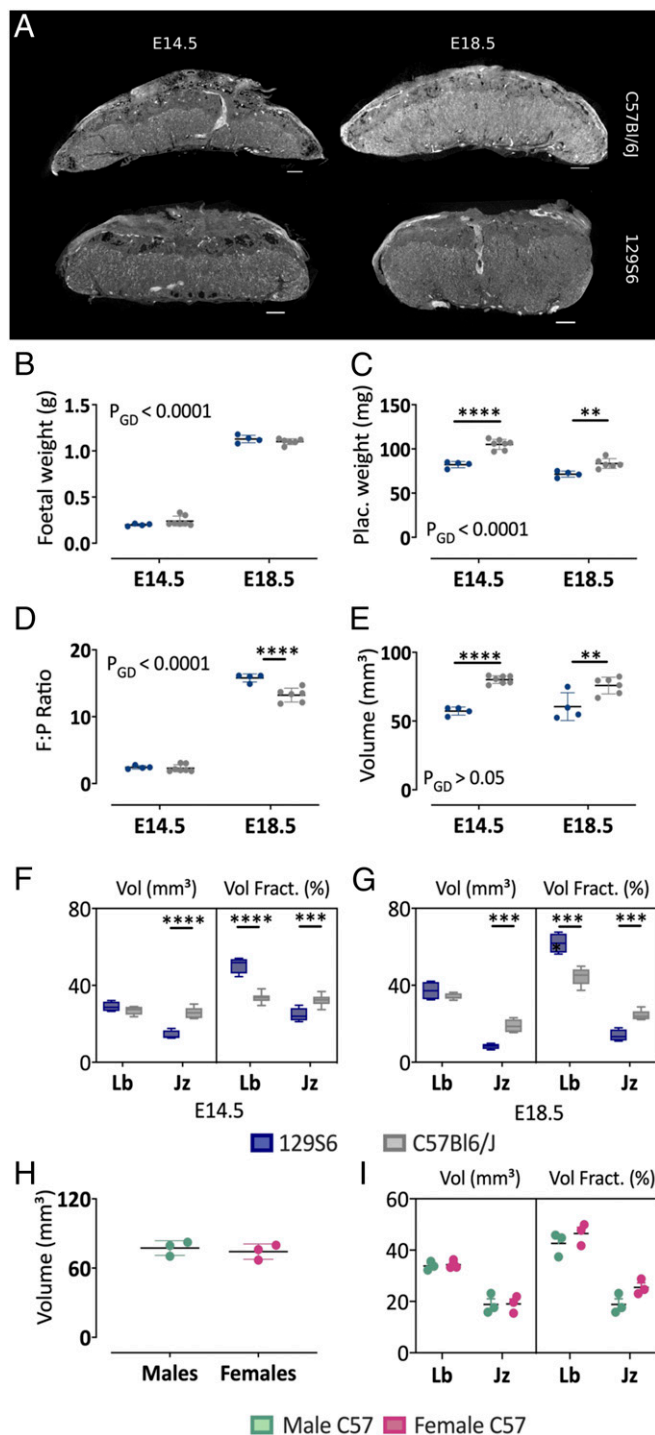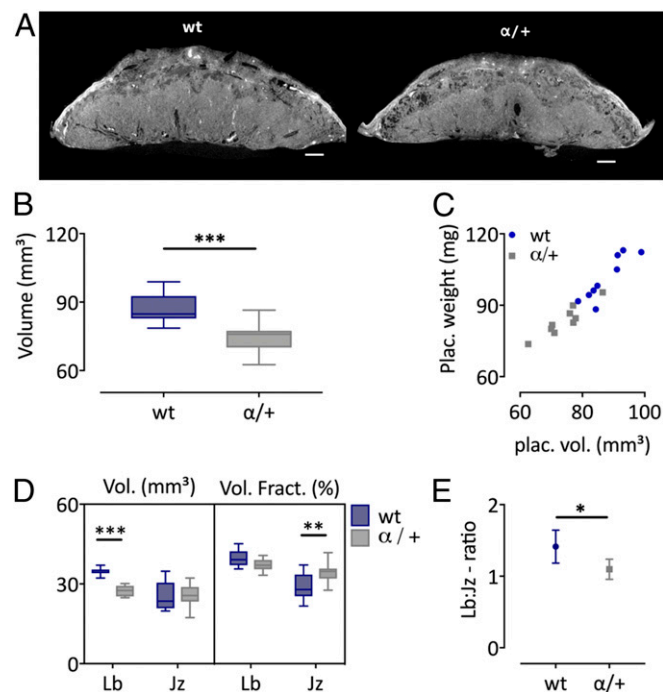

Fig. 5. Morphometric comparison of C57BL/6J and 129S6 placentas using Zr-POM-based CE-CT. (A) Representative CE-CT image of a placenta isolated at E14.5 and E18.5 from C57BL/6J and 129S6 mice. (Scale bar, 500 μm.) (B) Fetal weight, (C) placental weight, (D) placental efficiency as fetal:placental weight (F:P) ratios, and (E) placental volume at E14.5 and E18.5. Volume and the volume fraction of the junctional zone (Jz) and labyrinth (Lb) at (F) E14.5 and (G) 18.5. (H) Placental volumes of male versus female placentas from C57BL/6J mice at E18.5. (I) Volume and volume fraction of junctional zone and labyrinth in male versus female placentas. Statistical comparison with two-way ANOVA adjusted with Sidak's multiple comparison test (A, G, and I) or Mann–Whitney test (H). *P < 0.05, **P < 0.01, ****P < 0.0001. P$_{GD}$ = P value for the effect of the gestational day. Jz, junctional zone; Lb, labyrinth. N = 4 129S6 placentas from 3 litters and n = 6–7 C57BL/6J placentas from 3 litters per gestational day.

Fig. 6. Morphometric comparison of wt and PI3K α/+ mutants at E16. (A) Representative CE-CT image of a placenta from wt and α/+ littermates. (Scale bar, 500 μm.) (B) Placental volume determined by CE-CT, unpaired t test. (C) Correlation between placental weight and volume. (D) Volume and the volume fraction of the junctional zone (Jz) and labyrinth (Lb), two-way ANOVA adjusted with Sidak's multiple comparison test. (E) Lb:Jz ratio shown as mean ± 95% coincidence interval, unpaired t test. N = 9 samples from 5 litters/group. *P < 0.05, **P < 0.01, ***P < 0.001. Jz, junctional zone; Lb, labyrinth.

blood and the spatial resolution of 3.5 μm limited complete separation of fetal and maternal vasculature (*SI Appendix*, Fig. S6) and require further optimization. Nevertheless, using Zr-POM–based CE-CT, an initial inspection of the uteroplacental vasculature can be performed.

Visualization of placental pathologies.

Embryo resorption. Embryonic resorption is a natural process that occurs in up to 30–40% of the litter (38). Here we visualized and analyzed the placenta from resorbed embryos retrieved at E15.5 and E17.5 of 129S6 mice (Fig. 7 *A–C*). The placenta isolated at E15.5 had a volume of 40.5 mm^3, of which the labyrinth comprised 44.7% and the junctional zone 21.5%. It therefore had a Lb:Jz ratio of ~2. These placental volumes however, did not correspond to a typical E15.5 placenta (Fig. 4), and the morphology of the junctional zone was affected (Movie S4). In contrast, the placenta of the resorption found at E17.5 showed clear placental defects in the labyrinth, including dilated blood spaces (Fig. 7*B*). The placental volume was 45.9 mm^3 and consisted of 50.7% labyrinth and 25.7% junctional zone, resulting in a Lb:Jz ratio of ~2 as well. The placental characteristics of the 2 resorption sites resembled the morphological features that are typical for E14.5 placentas with volumes ranging between 47 and 53 mm^3; labyrinth and junctional proportions of 43–55% and 20–29%, respectively; and average ratio values of about 2. These findings might suggest that placental development arrested in both conceptuses around E14.5. Although both fetuses were severely growth restricted, we observed different pathologies in each. In the E15.5 fetus, the resorption was advanced, and there were clear signs of degrading tissue apparent in the upper part of the fetal body (*SI Appendix*, Fig. S7A). In contrast, the anatomy of the fetus found at E17.5 was intact, although retarded in development (*SI Appendix*, Fig. S7B). Indeed, both forelimb as hind limb buds were formed, but no digits could be distinguished, implying that development halted around Theiler stage 19–20 (corresponding to E11.5–E12.5). These findings exemplified the ease of examining the pathology of embryonic resorptions by Zr-POM–based CE-CT.

Monochorionic and dichorionic twin placentas. Fused placentas and twin placentas are rarely observed phenomena in mice. Coincidentally,

a fused placenta was retrieved at the cervical pole of an E18.5 C57BL/6J female, with an overall weight of 174 mg (Fig. 7*D*). Although both embryos retained their own amniotic sac, one fetus was severely growth restricted, while the other showed a normal body weight (0.699 vs. 1.05 g). Using CE-CT, the volume fractions of the placental layers were evaluated. Interestingly, the placentas were fused at the junctional zone, suggesting that each fetus retained its own fetoplacental vasculature and this was a dichorionic, diamniotic twin pregnancy. However, unequal placental sharing was observed as the growth restricted fetus appropriated only 42% of the placenta. The volume fractions of both parts of the placenta were similar (~40% labyrinth and ~30% junctional zone), suggesting that placentation was not affected per se (Fig. 7*F*). However, the small placenta seemingly had more maternal blood pools in the decidua, an increased number of spiral arteries, and more junctional zone inclusions in the labyrinth compared with the larger placenta (Movie S5).

In addition, a monoamniotic twin placenta was retrieved at E18.5 of a C57BL/6J female, in which both embryos resided within 1 amniotic sac. One fetus had a normal appearance and bodyweight for its gestational age (1.05 g), whereas the other fetus was severely compromised and underdeveloped (bodyweight ~0.7 g). The placenta had an overall weight of 191 mg that corresponded to a volume of 140 mm^3, of which the labyrinth was 70 mm^3 and the junctional zone 43 mm^3. Notably, 2 clearly distinguishable insertion sites of the umbilical cord were observed (Fig. 7*D* and *SI Appendix*, Fig. S8). Although there were pronounced inclusions of the junctional zone within the labyrinth in the middle of the placenta, the separation was not absolute as was observed in the fused placentas, indicating a monochorionic twin pregnancy. These findings suggest that the blood supply of the fetuses might have been connected, which may have led to the twin–twin transfusion syndrome. Overall, CE-CT offered the ability to quickly discriminate between placental fusion or monoamniotic twin placentas.

Embryonic development. Finally, the anatomy and development of fetuses can be visualized by the incubation of Zr-POM. As such, all vital organs can be inspected and measured in detail, including the lungs, the heart, and the liver (*SI Appendix*, Fig. S9 and Movie S6). In conclusion, these results suggest that Zr-POM–based CE-CT holds great value to visualize tissue morphology at different stages of the embryonic development, allowing for rapid 3D histology.

Discussion

New applications for the use of microCT in biomedical sciences are being described constantly. In addition, visualization of soft tissues by diffusion of contrast agents has contributed to its popularity and makes microCT very valuable to obtain volumetric data of various tissues. Indeed, CE-CT was recently implemented as a high-throughput tool for morphological analysis of mouse development (27). Although the authors discussed the option to analyze placental development, no quantification of morphological features was performed. However, it was recently described that placental defects are present in almost all mutant strains that die before E14.5 (3), highlighting the importance of inspecting extraembryonic tissue in new mutant strains. Indeed, failure to appreciate placental defects has resulted in the misconception of gene function during development. Initial analysis of the murine placenta involves measuring the areas of the placental layers on histological sections (12). However, layered structures such as the placenta are prone to anisotropic and nonuniform deformation during tissue processing, which is, withal, a process that is sample specific (39). Quantification of areas on a selected number of slides is therefore merely correct when this is estimated from exhaustive sectioning and stereological analysis. In this study, we validated the use of Zr-POM–based CE-CT as a tool for fast, simple, and robust visualization and quantification of the placental morphology.
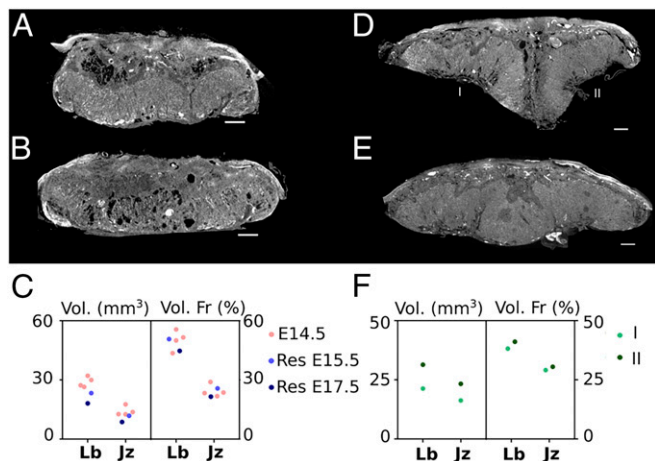

Fig. 7. Visualization and quantification of biological variances in placenta. (*A*) CE-CT cross section of the placenta isolated from a resorbed 129S6 embryo at E15.5. (*B*) CE-CT cross section of the placenta isolated from a resorbed 129S6 embryo at E17.5. (*C*) Quantification of the absolute volume and the volume fraction of the placentas (labyrinth [Lb] and junctional zone [Jz]) from resorbed embryos, compared with the characteristics of an E14.5 placenta. (*D*) CE-CT cross section of a fused placenta from a C57BL/6J mouse at E18.5. (*E*) CE-CT cross section of a twin placenta from a C57BL/6J mouse at E18.5. (*F*) Quantification of the absolute volume and the volume fraction of the 2 parts of the fused placentas. (Scale bar, 500 μm.)

Visualization of Placental Development. Using Zr-POM–based CE-CT, we were able to image early embryonic development, as well as placentation from E7.5 until term. Indeed, distinct features of the late primitive streak embryo were apparent at E7.5, such as the 3 cavities, separated by the chorion and the amnion, the ecto-placental cone, and the allantoic bud. At E8.5, somite formation and the first signs of chorioallantoic attachment were visible. Therefore, CE-CT could be applied to evaluate whether allantois formation is delayed or whether chorioallantoic attachment occurred. At E9.5, embryo turning and closure of the neural tube could be observed. Interestingly, using our techniques we detected that 1 embryo imaged was developmentally delayed by 1 d. In particular, although chorioallantoic fusion had occurred, embryo turning was not complete, and somite formation was halted.

The definitive mouse placenta and its dynamic changes in structure could be imaged from E10.5 by Zr-POM–based CE-CT. Moreover, the structural characteristics of the placenta provided sufficient contrast to delineate the individual placental layers, as verified by histology. Indeed, the high correlation between the area of the labyrinth measured on the CE-CT image and its corresponding histological section granted evidence that placental layers can be delineated by CE-CT to perform volume quantification in a straightforward fashion. In addition, we observed large variations in 2D labyrinth to junctional zone ratios of sections that were perpendicular, although in the center of the placenta. Thus, using intact samples in Zr-POM–based CE-CT offers the distinct advantage of enabling 3D ratiometric measures that are not prone to sample bias.

Finally, Zr-POM incubation enabled the development of fetuses to be examined by CE-CT as well. As such, the soft and mineralized tissues of an E18.5 embryo could be visualized and allowed the quantification of organs of interest. Obtaining volumetric measurements of vital organs, such as the brain and liver, in the fetus offers the additional potential to assess the symmetry of fetal growth. This is particularly useful as the aetiologies and perinatal outcomes are believed to vary between fetuses that are symmetrically versus asymmetrically growth restricted (40). In addition, this technique offers the possibility to explore how placental defects might be associated with fetal organ development. However, visualization of fetal development by CE-CT has been described previously (27) and therefore is not further discussed.

Quantification of Placental Development. The overall placental volume determined by Zr-POM–based CE-CT was significantly correlated with placental weight. Placental density, defined as weight per volume, showed no marked differences between the gestational ages studied. Nevertheless, substantial differences in placental structure between C57BL/6J and 129S6 mice were translated in altered density values. Therefore, calculating this parameter might be useful in identifying where there may be a disconnection between placental growth and structural changes in pathological mouse pregnancies. Moreover, measurements of placental density in human placentas could be used to predict pregnancy complications before delivery, assuming volume and weight measurements from ultrasound (41).

In line with stereological assessments of the C57BL/6J placenta (10), the absolute volume and volume fraction of the placental labyrinth zone determined by Zr-POM–based CE-CT also increased toward term in 129S6 placentas. These ontogenic changes are also consistent with the increasing demands for nutrient exchange by the placenta to cope with exponential fetal growth. On the contrary, the absolute and fractional volumes of the junctional zone and decidua decreased over time. Attaining volume quantities of the placental layers by Zr-POM–based CE-CT provided the possibility to determine the true 3D labyrinth to junctional zone ratio, which was not section dependent. Moreover, other morphological features of the placental layers could also be visualized with Zr-POM–based CE-CT. In particular, the proportion of glycogen cells and spongiotrophoblast cells in the junctional zone

could be evaluated because of the difference in cellular composition. This presents the opportunity to assess the volume of glycogen cells in cases of placental hypo/hyperplasia or in complicated pregnancies such as gestational diabetes mellitus and intrauterine growth restriction (42). Similar to what is described in previous studies (33), the amount of glycogen cells residing in the junctional zone decreased significantly toward term. Although the migration of the glycogen into the maternal decidua could not be readily visualized, defects in migration may be indirectly inferred if more glycogen cells were resident within the junctional zone. Additionally, this research tool offers the opportunity to quantify ectopic inclusions of the junctional zone in the labyrinth, in terms of number, size, and cellular composition. Indeed, observing an increased abundance of these ectopic inclusions in the labyrinth may reflect defects in placental development (34). However, secondary trophoblast giant cells, which compose an additional cell population of the junctional zone, were not identifiable. In contrast, primary trophoblast giant cell layers enclosing the conceptus at E8.5 were distinguishable from the surrounding decidua. Apart from its possibilities, the study would benefit from further optimization. Most likely, the standard image processing algorithms used in this study are not sufficient to acquire all information from the images, and more advanced techniques, such as machine or deep learning, could result in more accurate quantifications. In addition, comparing the CE-CT images with corresponding histological sections of the same sample required detailed comparison and interpolation of the CE-CT dataset. One method to overcome this may be to subject the CE-CT–imaged samples to further processing by tissue clarification and immune-labeling. Using this approach, 3D constructions of CE-CT–scanned sample could be compared with the 3D construction of the immune-labeled cleared sample (43, 44).

Critical to fetal survival is the reciprocal exchange of gases, nutrients, and waste between mother and fetus. Spiral arteries from the maternal decidua coalesce at the border of the junctional zone into 1 to 4 central canals that shunt maternal blood to the bottom of the labyrinth. The oxygen-poor fetal blood flows via arterioles into labyrinth where they extensively branch into dense capillaries, which drain the oxygen-rich blood back toward the fetus. In mice, the maternal blood is separated from fetal blood by a trilaminar interhaemal membrane that comprises fetal endothelial cells and 2 syncytiotrophoblast layers. Here the affinity of Zr-POM for blood enabled the visualization of the placental vasculature in CE-CT without additional intravascular infusion of contrast agents. In particular, we observed that the diameter of the uterine canals increased from E13.5 to E17.5, which is in line with previous reports (37). Additionally, focal hemorrhage could also be easily detected. Disadvantageously, the visualization of blood vessels depended on blood to be retained within the vessels. Moreover, the spatial resolution in this study (3.5 μm) was insufficient to completely separate the 2 vasculatures since the minimum thickness of the interhaemal membrane is 4.8 μm near term (11). Thus, additional work is required to optimize the image analysis software to allow accurate assessment of the labyrinth exchange interface. Nevertheless, detailed analysis of the utero-placental and fetoplacental vasculature has been described previously by the use of i.v. contrast agents in mouse and human placentas (45). Although these methods can be used to obtain hemodynamic insights, capillaries cannot be visualized, and information on the basic placental morphology cannot be attained. Therefore, it might be promising to combine i.v. applied contrast agent to stain larger blood vessels and Zr-POM to visualize morphology and the residual blood within the capillaries. Alternatively, optimizing sample preparation for Zr-POM–based CE-CT such that the placental vessels remain filled with blood, may improve branching analysis. Although not assessed in this study, this feature may also be exploited to assess the extent of spiral artery remodeling at the fetomaternal interface as this is important for successful pregnancy.

Biological and Genetic Variation of Placentas. The 129S6 and C57BL/6J mice are the 2 most popular mouse strains used in laboratories. Interestingly, embryonic lethality and placental defects are often strain dependent. Here we exploited the fact that genetic background affects placental morphology to validate the ability of Zr-POM–based CE-CT to quantify placental volumes (30). In line with literature, we observed significantly larger placental volume, as well as an increased volume fraction of the junctional zone but a decreased labyrinth volume fraction in C57BL/6J mice compared with 129S6 using CE-CT. This significantly smaller exchange surface might explain the reduced placental efficiency of C57BL/6J placentas and might impose a more sever phenotype in mutants that affect labyrinth functioning. Recently, sexual dimorphic differences in placental phenotypes are being described (46, 47). This area still being in its infancy, it remains unclear whether placental volume fractions are different in placentas from wild-type male and female fetuses. In this study, no differences were observed in either placental volume or volume fraction at E18.5 placentas from C57BL/6J mice. These findings are in line with stereological assessments of rat placentas where sexual dimorphic differences observed at midgestation were no longer present at E20 (48). These findings confirm the striking difference in placental morphology between mouse strains and validate the use of the Zr-POM CE-CT methodology.

In addition, the use of Zr-POM–based CE-CT to detect placental defects was assessed in a model with known placental malfunction. Pups that are heterozygous deficient for the PI3K isoform, p110α (α/+), are growth restricted as a result of a smaller placenta and defective labyrinth zone formation (31). Consistent with this, we also observed significantly smaller placental volumes and a reduced labyrinth volume in α/+ mutants compared with wild-type littermates using the CE-CT technique. These findings would prompt a detailed inspection of the labyrinth exchange region. Indeed, using stereology, the authors showed that fetal capillary volume and length, exchange surface area, and diffusion capacity were all decreased in α/+ mutants (31).

Apart from differences between different mouse strains, striking variations were also observed in naturally occurring resorption sites. Placental volumes were analyzed from placentas of resorbed conceptuses, which were severely growth restricted and demised at E15.5 and E17.5. Interestingly, both placentas had structural characteristics that resembled E14.5 placentas, suggesting that placental development did not progress past E14.5. Impaired junctional morphology was observed in the E15.5 placenta, and embryonic resorption was clearly ongoing. In contrast, the placenta isolated at E17.5 had dilated blood spaces in the labyrinth and disturbed placental morphology since the volume fraction of the labyrinth was reduced compared with a normal E17.5 placenta. These findings might indicate that proper functioning of both the labyrinth, as well as the junctional zone, is important for normal development.

Fusion of placentas from neighboring embryos is a rare phenomenon with an estimated frequency of less than 1%. It is thought to result from aberrant embryo spacing or overcrowding, which leads to competition for nutrients and space between neighboring conceptuses and, ultimately, impaired fetal development (49, 50). We examined a fused placenta of 2 conceptuses by Zr-POM–based CE-CT, one having normal fetal weight for an E18.5 embryo, while the other was severely growth restricted (being 50% smaller). Given the advantage of CE-CT to obtain 3D histological data, the morphology of the fused placentas could be easily examined. Interestingly, each conceptus retained their own labyrinth, whereas the junctional zones were fused in the middle. This implied that the growth restriction of the small conceptus was not caused by unbalanced blood flow from one fetus to the other. Nevertheless, we did observe a disproportionate distribution of the placental mass with the normally growing fetus supported by 58% of the fused placenta. Moreover, the volumes of the labyrinth and the junctional zone were higher for the normal weight fetus. However, the volume fractions of the placental regions were very similar between the normal weight and growth restricted fetus, resulting in similar zonal ratios. These findings suggest that placentation per se was not affected, but competition for space and nutrients impacted normal placental growth and thus fetal growth. Interestingly, there were many large blood vessels in the maternal decidua covering the smaller of the fused placentas. This may reflect an attempt of the mother to compensate and increase resource supply to the conceptus, although this was insufficient to maintain normal growth.

Finally, we observed a placenta with 2 umbilical cords and a labyrinth that was seemingly not separated per fetus. This could imply that fetal blood supplies were connected, which posed a risk of unbalanced blood flow and might result in twin–twin transfusion syndrome. Although our current analyses were unable to identify vessels that linked the blood flow between the twins, 1 twin suffered from poor nourishment and hence fetal demise.

Taken together, this study illustrated the use of Zr-POM–based CE-CT to assess mouse placental development and its most common defects, including failure of chorioallantoic attachment, a small placenta, distorted placental structure, junctional zone inclusions in the labyrinth, underdeveloped labyrinth, disorganized junctional zone, the presence of fibrotic or necrotic areas, and dilated blood spaces. Indeed, CE-CT offers a nondestructive, quantitative, and robust technique to evaluate, within 1 dataset, different placental parameters like the total volume, volume fractions, ratio of different placental layers, and volumes of specific cell populations. Moreover, this research tools allows the inspection of the vasculature within the entire placenta, as well as identifying placental defects in embryonic resorption and placental fusion pathologies. Collectively, the possibility of multisample holders, in addition to the ease of the technique and the high spatial resolution, render Zr-POM–based CE-CT as a promising tool that can be automated for high-throughput screening of structural defects. Indeed, Zr-POM–based CE-CT offers the advantage to inspect the 3D structure of the placenta and has an immense complementary value to histology

Materials and Methods

Mice. All animal experiments were approved by the Ethical Committee of the Faculty of Biomedical Sciences of the KU Leuven. Mice were housed in filtertop cages under conventional conditions and kept under controlled conditions. Eight- to 12-wk-old 129S6 inbred mice were obtained from an internal breeding program. C57BL/6J inbred mice were obtained from Janvier. The PI3K p110α mice were bred in the University of Cambridge Animal Facility abiding by the UK Home Office Animals (Scientific Procedures) Act 1986, and local ethics committee and genotyping was performed as previously described (31). Mice were mated, and the detection of a copulation plug was dated as E0.5 of pregnancy. Unless mentioned otherwise, samples were isolated, fixed in 4% PFA for 24 h, and stored in Dulbecco's PBS (DPBS; Gibco). Placentas from E10.5 and E11.5 were isolated with the mesometrial triangle. Yolk sac and fetal membranes were removed after isolation before measuring placental weight. For the visualization of the early development, implantation sites from E7.5 to E9.5 were isolated within the myometrium and decidual tissue. Fetuses of E18.5 were euthanized by i.p. injection of ketamine/xylazine (300 mg/kg + 30 mg/kg), fixed in 4%PFA for 48 h, and stored in DPBS. Small slices were made in the skin to improve diffusion of the contrast agent. Only animals with litters of more than 4 fetuses were included in the study.

Contrast-Enhanced CT.

Contrast agent. The contrast agent used was a zirconium-substituted Keggin polyoxometalate (51): ((Et$_2$NH$_2$)$_{10}$[Zr(PW$_{11}$O$_{39}$)$_2$]·7H$_2$O). The Zr-POM has a net charge of −10 (the metal ion +4 and the polyoxometalate −14) and a molecular weight of 6,313.43 g/mol. Placental samples were incubated for at least 7 d, and fetuses for 28 d, in the contrast solution (35 mg per ml PBS), while gently shaking (50 rpm) at room temperature.

CE-CT acquisition. Placentas were scanned in PBS using a Phoenix Nanotom M (GE Measurement and Control Solutions) at 3.5 μm (129S6) or 4.5 μm (C57BL/6J) isotropic voxel size. The source, equipped with a tungsten target, was operated at 60 kV and 240 μA. An aluminum filter of 0.1 mm was applied to reduce beam

hardening. For each sample, 2,400 frames were acquired over 360° using the fast scan mode with an exposure time of 500 ms (frame averaging = 1 and image skip = 0) (26), resulting in a scanning time of only 20 min per sample.

Fetuses were scanned in PBS at 7 μm isotropic voxel size at 60 kV and 300 μA, using a 0.2-mm aluminum filter. To visualize the complete fetus, a multiscan approach was applied. For each scan, 1,800 frames were acquired over 360° with an exposure time of 500 ms (frame averaging = 3 and image skip = 1), resulting in a total scan time of 2 h 45 min.

Afterward, scan optimization (projection filter, inline volume filter, and beam hardening correction) was applied during 3D reconstruction (Datos|x, GE Measurement and Control solutions).

Data Display and Statistics. Graph display and statistics were done in Graphpad Prism (Graphpad Software). Normality was assessed with D'Agostino and Pearson omnibus normality test. Data were analyzed with Mann–Whitney test, Kruskal–Wallis multiple comparison test with Dunn's corrections or two-way ANOVA test with Dunnet's corrections. Correlations were tested with Pearson correlation test or the nonparametric Spearman correlation test. Differences were considered statistically significant when $P < 0.05$. Boxplots displayed median with first and third quartile with whiskers at the minimum and maximum values. Data display and 3D rendering of the CE-CT images were done by Dataviewer and CTvox (Bruker MicroCT).

1. A. Ayadi et al., Mouse large-scale phenotyping initiatives: Overview of the European Mouse Disease Clinic (EUMODIC) and of the Wellcome Trust Sanger Institute Mouse Genetics Project. Mamm. Genome 23, 600–610 (2012).
2. M. E. Dickinson et al.; International Mouse Phenotyping Consortium; Jackson Laboratory; Infrastructure Nationale PHENOMIN, Institut Clinique de la Souris (ICS); Charles River Laboratories; MRC Harwell; Toronto Centre for Phenogenomics; Wellcome Trust Sanger Institute; RIKEN BioResource Center, High-throughput discovery of novel developmental phenotypes. Nature 537, 508–514 (2016).
3. V. Perez-Garcia et al., Placentation defects are highly prevalent in embryonic lethal mouse mutants. Nature 555, 463–468 (2018).
4. E. J. Camm, K. J. Botting, A. N. Sferruzzi-Perri, Near to one's heart: The intimate relationship between the placenta and fetal heart. Front. Physiol. 9, 629 (2018).
5. D. J. Barker, C. Osmond, J. Golding, D. Kuh, M. E. Wadsworth, Growth in utero, blood pressure in childhood and adult life, and mortality from cardiovascular disease. BMJ 298, 564–567 (1989).
6. A. A. Vaag, L. G. Grunnet, G. P. Arora, C. Brøns, The thrifty phenotype hypothesis revisited. Diabetologia 55, 2085–2088 (2012).
7. T. Napso, H. E. J. Yong, J. Lopez-Tello, A. N. Sferruzzi-Perri, The role of placental hormones in mediating maternal adaptations to support pregnancy and lactation. Front. Physiol. 9, 1091 (2018).
8. J. Mu, S. L. Adamson, Developmental changes in hemodynamics of uterine artery, utero- and umbilicoplacental, and vitelline circulations in mouse throughout gestation. Am. J. Physiol. Heart Circ. Physiol. 291, H1421–H1428 (2006).
9. J. Rossant, J. C. Cross, Placental development: Lessons from mouse mutants. Nat. Rev. Genet. 2, 538–548 (2001).
10. P. M. Coan, A. C. Ferguson-Smith, G. J. Burton, Developmental dynamics of the definitive mouse placenta assessed by stereology. Biol. Reprod. 70, 1806–1813 (2004).
11. P. M. Coan, A. C. Ferguson-Smith, G. J. Burton, Ultrastructural changes in the interhaemal membrane and junctional zone of the murine chorioallantoic placenta across gestation. J. Anat. 207, 783–796 (2005).
12. D. R. Natale, M. Starovic, J. C. Cross, Phenotypic analysis of the mouse placenta. Methods Mol. Med. 121, 275–293 (2006).
13. C. V. Howard, M. Reed, Volume and surface-area estimation from microscopic images. J. Microsc. 190, 291 (1998).
14. H. J. Gundersen, E. B. Jensen, The efficiency of systematic sampling in stereology and its prediction. J. Microsc. 147, 229–263 (1987).
15. T. M. Mayhew, G. J. Burton, Stereology and its impact on our understanding of human placental functional morphology. Microsc. Res. Tech. 38, 195–205 (1997).
16. I. Kallai et al., Microcomputed tomography-based structural analysis of various bone tissue regeneration models. Nat. Protoc. 6, 105–110 (2011).
17. M. L. Bouxsein et al., Guidelines for assessment of bone microstructure in rodents using micro-computed tomography. J. Bone Miner. Res. 25, 1468–1486 (2010).
18. M. Marxen et al., MicroCT scanner performance and considerations for vascular specimen imaging. Med. Phys. 31, 305–313 (2004).
19. L. Chi et al., G9a controls placental vascular maturation by activating the Notch Pathway. Development 144, 1976–1987 (2017).
20. A. Rai, J. C. Cross, Development of the hemochorial maternal vascular spaces in the placenta through endothelial and vasculogenic mimicry. Dev. Biol. 387, 131–141 (2014).
21. M. Y. Rennie, A. Rahman, K. J. Whiteley, J. G. Sled, S. L. Adamson, Site-specific increases in utero- and fetoplacental arterial vascular resistance in eNOS-deficient mice due to impaired arterial enlargement. Biol. Reprod. 92, 48 (2015).
22. M. Y. Rennie et al., Vessel tortuousity and reduced vascularization in the fetoplacental arterial tree after maternal exposure to polycyclic aromatic hydrocarbons. Am. J. Physiol. Heart Circ. Physiol. 300, H675–H684 (2011).
23. Y. J. Zhou, M. L. Yuan, R. Li, L. P. Zhu, Z. H. Chen, Real-time placental perfusion on contrast-enhanced ultrasound and parametric imaging analysis in rats at different gestation time and different portions of placenta. PLoS One 8, e58986 (2013).
24. A. C. Langheinrich et al., Quantitative 3D micro-CT imaging of the human fetoplacental vasculature in intrauterine growth restriction. Placenta 29, 937–941 (2008).
25. T. O. Junaid, R. S. Bradley, R. M. Lewis, J. D. Aplin, E. D. Johnstone, Whole organ vascular casting and microCT examination of the human placental vascular tree reveals novel alterations associated with pregnancy disease. Sci. Rep. 7, 4144 (2017).
26. G. Kerckhofs et al., Changes in bone macro- and microstructure in diabetic obese mice revealed by high resolution microfocus X-ray computed tomography. Sci. Rep. 6, 35517 (2016).
27. C. W. Hsu et al., Three-dimensional microCT imaging of mouse development from early post-implantation to early postnatal stages. Dev. Biol. 419, 229–236 (2016).
28. G. Kerckhofs et al., Simultaneous three-dimensional visualization of mineralized and soft skeletal tissues by a novel microCT contrast agent with polyoxometalate structure. Biomaterials 159, 1–12 (2018).
29. J. Buytaert, J. Goyens, D. De Greef, P. Aerts, J. Dirckx, Volume shrinkage of bone, brain and muscle tissue in sample preparation for micro-CT and light sheet fluorescence microscopy (LSFM). Microsc. Microanal. 20, 1208–1217 (2014).
30. S. J. Tunster, M. Van de Pette, R. M. John, Impact of genetic background on placental glycogen storage in mice. Placenta 33, 124–127 (2012).
31. A. N. Sferruzzi-Perri, J. López-Tello, A. L. Fowden, M. Constancia, Maternal and fetal genomes interplay through phosphoinositol 3-kinase(PI3K)-p110α signaling to modify placental resource allocation. Proc. Natl. Acad. Sci. U.S.A. 113, 11255–11260 (2016).
32. C. Armit et al., eMouseAtlas: An atlas-based resource for understanding mammalian embryogenesis. Dev. Biol. 423, 1–11 (2017).
33. P. M. Coan, N. Conroy, G. J. Burton, A. C. Ferguson-Smith, Origin and characteristics of glycogen cells in the developing murine placenta. Dev. Dyn. 235, 3280–3294 (2006).
34. C. Rampon et al., Protocadherin 12 deficiency alters morphogenesis and transcriptional profile of the placenta. Physiol. Genomics 34, 193–204 (2008).
35. S. L. Adamson et al., Interactions between trophoblast cells and the maternal and fetal circulation in the mouse placenta. Dev. Biol. 250, 358–373 (2002).
36. D. G. Simmons, "Postimplantation development of the chorioallantoic placenta" in The Guide to Investigate Mouse Pregnancy, B. A. Croy, A. T. Yamads, F. J. DeMayo, S. L. Adamson, Eds. (Elsevier, 2014).
37. B. K. Yadav et al., A longitudinal study of placental perfusion using dynamic contrast enhanced magnetic resonance imaging in murine pregnancy. Placenta 43, 90–97 (2016).
38. L. E. Flores, T. B. Hildebrandt, A. A. Kühl, B. Drews, Early detection and staging of spontaneous embryo resorption by ultrasound biomicroscopy in murine pregnancy. Reprod. Biol. Endocrinol. 12, 38 (2014).
39. K. A. Dorph-Petersen, J. R. Nyengaard, H. J. Gundersen, Tissue shrinkage and unbiased stereological estimation of particle number and size. J. Microsc. 204, 232–246 (2001).
40. J. S. Dashe, D. D. McIntire, M. J. Lucas, K. J. Leveno, Effects of symmetric and asymmetric fetal growth on pregnancy outcomes. Obstet. Gynecol. 96, 321–327 (2000).
41. H. S. Kim, S. H. Cho, H. S. Kwon, I. S. Sohn, H. S. Hwang, The significance of placental ratios in pregnancies complicated by small for gestational age, preeclampsia, and gestational diabetes mellitus. Obstet. Gynecol. Sci. 57, 358–366 (2014).
42. L. K. Akison, M. D. Nitert, V. L. Clifton, K. M. Moritz, D. G. Simmons, Review: Alterations in placental glycogen deposition in complicated pregnancies: Current preclinical and clinical evidence. Placenta 54, 52–58 (2017).
43. G. Merz, V. Schwenk, R. G. Shah, P. Necaise, C. M. Salafia, Clarification and 3-D visualization of immunolabeled human placenta villi. Placenta 53, 36–39 (2017).
44. K. Kagami, Y. Shinmyo, M. Ono, H. Kawasaki, H. Fujiwara, Three-dimensional visualization of intrauterine conceptus through the uterine wall by tissue clearing method. Sci. Rep. 7, 5964 (2017).
45. M. Y. Rennie, K. J. Whiteley, S. Kulandavelu, S. L. Adamson, J. G. Sled, 3D visualisation and quantification by microcomputed tomography of late gestational changes in the arterial and venous feto-placental vasculature of the mouse. Placenta 28, 833–840 (2007).
46. A. Wieczorek et al., Sex-specific regulation of stress-induced fetal glucocorticoid surge by the mouse placenta. Am. J. Physiol. Endocrinol. Metab., 10.1152/ajpendo.00551.2018 (2019).
47. J. I. Kalisch-Smith, D. G. Simmons, H. Dickinson, K. M. Moritz, Review: Sexual dimorphism in the formation, function and adaptation of the placenta. Placenta 54, 10–16 (2017).
48. J. I. Kalisch-Smith, D. G. Simmons, M. Pantaleon, K. M. Moritz, Sex differences in rat placental development: From pre-implantation to late gestation. Biol. Sex Differ. 8, 17 (2017).
49. Q. Chen et al., Transient beta2-adrenoceptor activation confers pregnancy loss by disrupting embryo spacing at implantation. J. Biol. Chem. 286, 4349–4356 (2011).
50. J. G. Carr, Placental fusion in mice. Proc. R. Soc. Edinb. Biol. 62, 189 (1946).
51. H. G. T. Ly, T. N. Parac-Vogt, Spectroscopic study of the interaction between horse heart myoglobin and zirconium(IV)-substituted polyoxometalates as artificial proteases. ChemPhysChem 18, 2451–2458 (2017).